npj | computational materials

Article

Published in partnership with the Shanghai Institute of Ceramics of the Chinese Academy of Sciences

https://doi.org/10.1038/s41524-024-01220-x

Crystal net catalog of model flat band materials

Paul M. Neves [1], Joshua P. Wakefield [1], Shiang Fang [1], Haimi Nguyen[2,3], Linda Ye [1,4] & Joseph G. Checkelsky [1]

Flat band systems are currently under intense investigation in quantum materials, optical lattices, and metamaterials. These efforts are motivated by potential realization of strongly correlated phenomena enabled by frustration-induced flat band dispersions; identification of candidate platforms plays an important role in these efforts. Here, we develop a high-throughput materials search for bulk crystalline flat bands by automated construction of uniform-hopping near-neighbor tight-binding models. We show that this approach captures many of the essential features relevant to identifying flat band lattice motifs in candidate materials in a computationally inexpensive manner, and is of use to identify systems for further detailed investigation as well as theoretical and metamaterials studies of model systems. We apply this algorithm to 139,367 materials in the Materials Project database and identify 63,076 materials that host at least one flat band elemental sublattice. We further categorize these candidate systems into at least 31,635 unique flat band crystal nets and identify candidates of interest from both lattice and band structure perspectives. This work expands the number of known flat band lattices that exist in physically realizable crystal structures and classifies the majority of these systems by the underlying lattice, providing additional insights for familiar (e.g., kagome, pyrochlore, Lieb, and dice) as well as previously unknown motifs.

Flat band systems have recently received significant attention as platforms to realize exotic quantum states. Theoretically, the non-dispersive nature of these infinitely massive flat bands may enable electronic correlation effects, including ferromagnetism, high-temperature fractional quantum Hall physics, topological and/or high-temperature superconductivity, and excitonic insulating behavior[1–7]. The field of flat band physics has been recently invigorated by the experimental identification of flat electronic bands in 2D moiré heterostructures[8–13], bulk quantum materials[14,15], circuit QED systems[16], optical lattices[17], and photonic crystals[18]. Understanding the potential breadth of flat band platforms is thus a topic of significant interest.

Flat band-hosting crystal lattices were proposed over 30 years ago, exemplified by models for the kagome, Lieb, pyrochlore, and dice lattices[2,18–22] and the Penrose tiling[23]. Despite the apparent simplifications—e.g., being of nearest-neighbor, single orbital and isotropic nature—taken by these theoretical models, their relevance in describing electronic structures of real materials is supported by a growing number of experimental studies[14,15,24–31] and density functional theory (DFT) driven material searches[32]. This suggests that a simple tight-binding approach can provide key guidance for identifying additional flat band systems, even in the presence of other atomic species, spin-orbit coupling, orbital degrees of freedom, and interaction effects not taken into account at the tight-binding level. More recent theoretical efforts have expanded flat band models to more exotic lattices such as the diamond-octagon[33] and the Creutz[34–36], and introduced general models by which flat band lattices can be systematically generated such as via the line or split graph constructions[37–41]. In contrast to these broadened efforts, experimental realization in crystalline systems has been relatively scarce and has focused on the kagome prototype (e.g., refs. 14,24–31). There is therefore an opportunity to expand flat band studies with the identification of candidates for other lattice motifs, especially those that can be found in realistic material structures.

Here, we develop a high-throughput approach to identify flat band systems by building simple (i.e., nearest-neighbor, single orbital, uniform hopping) tight-binding models on candidates drawn from the Materials Project (MP). Motivated by the experimental observations of elementally derived flat bands in recent flat band studies[14,26], we then identify each elemental sublattice that hosts a non-trivial flat band originating from

[1]Department of Physics, Massachusetts Institute of Technology, Cambridge, MA 02139, USA. [2]Department of Physics, Mount Holyoke College, South Hadley, MA 01075, USA. [3]Present address: Department of Chemistry, Columbia University, New York, New York 10027, USA. [4]Present address: Division of Physics, Mathematics and Astronomy, California Institute of Technology, Pasadena, CA 91125, USA. e-mail: checkelsky@mit.edu

destructive interference of compact localized eigenstates (CLS) (Here, a trivial flat band is defined as one which is caused by a component of the lattice which is isolated from other components and does not contain any hopping paths to infinite distance)[42]. As the bandstructure of a uniform hopping model relies only upon the connectivity of the underlying periodic graph (the "crystal net"), we are able to categorize the majority of these systems by employing a crystal net isomorphism testing algorithm (Systre)[43] that generates a unique canonical key for each distinct crystal net. The remaining are grouped by invariant quantities of the sublattice graph and bandstructure (see methods section B and Supplementary Note 2). This allows us to identify the common flat band lattice motifs present in the MP, and to identify certain elements, spacegroups, and chemical structures that host candidates of a given flat band lattice, providing a broad set of flat band lattices for theoretical and experimental study. Note that when using this database to search for materials that are likely to host flat bands coming from the identified motif, further filtering based on chemical analysis and computational modeling is necessary, as only when the local site and orbital symmetries maintain the frustration of the *s*-orbital model will this flat band persist. Such an approach has proven successful in identifying flat band systems experimentally reported—see refs. 14,15,26 and Supplementary Note 7 and Supplementary Figs. 4–9.

Results

Search overview

The algorithm employed here is outlined in Fig. 1. For each material in the MP (e.g., $Bi_2Rh_3S_2$ in Fig. 1a), we consider each individual elemental sublattice within the crystal structure (Fig. 1c–e). For the shortest nearest-neighbor (NN) distance d_{NN} between any two atoms of this species in this structure, we identify all pairs of atoms in this sublattice less than or equal to a multiple χ of d_{NN} apart (depicted in Fig. 1b). Next, we build a tight-binding model with uniform self-energy and one orbital at each atomic site in the sublattice with hopping energy $t > 0$ between all site pairs $\langle i,j \rangle$ such that the site pair distance $d_{ij} < \chi d_{NN}$ (Fig. 1f–h):

$$H = -t \sum_{\langle i,j \rangle} \left(c_i^\dagger c_j + c_j^\dagger c_i \right). \quad (1)$$

c_i ($c_i^\dagger$) is the fermion creation (annihilation) operator at site i. We further define d_{NNN} as the shortest atomic distance greater than χd_{NN} (the shortest bond not included in the tight-binding model).

A search of 468,378 individual elemental sublattices from 139,367 materials in the MP for near-neighbor isotropic uniform hopping tight-binding flat bands was performed. The calculation was performed for χ cutoffs of 1.02, 1.05, 1.1, 1.2, and 1.4 (the statistics reported throughout this work include results of all listed choices of χ). 63,076 unique material entries were found to contain at least one non-trivially localized flat band across the entire 3D brillouin zone in at least one of their elemental sublattices for at least one value of χ. Some materials contain multiple decoupled lattice components (a component is defined as a connected subgraph that is not part of any larger connected subgraph) or multiple flat band lattices among different elemental sublattices in the same material; in total 108,341 flat band models were found within elemental sublattices. 15,288 unique flat band crystal nets were identified with Systre[43], while 68,710 components evaded classification in Systre due to barycentric node collisions (see methods). Applying lattice invariant based classification schemes identifies at least 16,347 additional crystal net groups, yielding at least 31,635 unique flat band crystal nets.

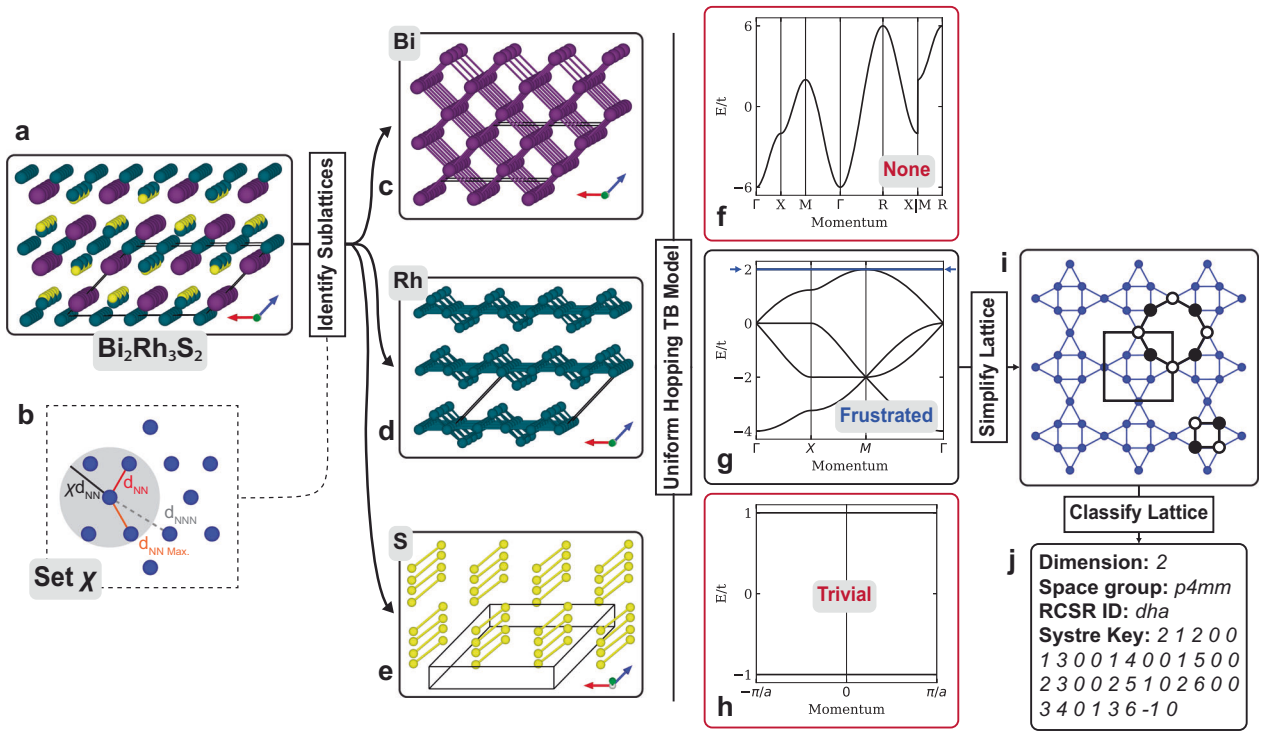

Fig. 1 | Flowchart of the tight-binding flat band search algorithm. a Structure of candidate $Bi_2Rh_3S_2$ (spacegroup *C*2/*m*, lattice parameters $a = 11.49$ Å, $b = 8.42$ Å, $c = 8.13$ Å, $\alpha = 90°$, $\beta = 133.45°$, and $\gamma = 90°$). **b** Nearest-neighbor (NN) distance d_{NN}, the bond length cutoff χd_{NN}, the longest distance included as a bond $d_{NN,max}$, and the shortest distance excluded as a next-nearest-neighbor (NNN) bond d_{NNN}. **c–h** The Bi lattice of $Bi_2Rh_3S_2$ supports no flat bands (**c**, **f**), while the S contains only trivially localized molecular flat bands (**e**, **h**). The Rh sublattice contains a non-trivial or frustrated two-dimensional flat band lattice with a doubly degenerate flat band at energy $E = 2t$ for hopping t which supports two distinct CLSs, the square kagome (or "squagome") lattice, identified as "dha" in the reticular chemistry structure resource[63] (**d**, **g**). **i** The squagome represented in high symmetry form, and **j** identified based on its Systre classification key. The unit cell of the squagome is shown with a black outline, and the two unique CLSs are shown with black and white lattice sites, indicating alternating signs of the wavefunction on each site (all other sites being zero).

Table 1 | Materials Statistics

Lattice	No. Materials
All	139,367
Have F.B.	63,076
Curated	2759
Kagome	5329
Pyrochlore	3700
Stub	3669
Diamond Chain	2557
Lieb	1976
Fluorite	1330
Kite	1291
Tetrahedron Chain	1131
Stub Honeycomb	1049
Hyperkagome	930

Statistics for the number of materials containing the most common flat band lattices.

Observed flat band motifs and abundances

In Table 1, we list in descending order the abundances of materials hosting the ten most common flat band lattices (the most common lattices and their tight-binding bandstructure are shown in Figs. 2 and 3, respectively, with additional common lattices shown in the Supplementary Fig. 2 and discussed in Supplementary Note 5). The kagome lattice is the most commonly identified lattice, found in 5329 materials (Figs. 2a, 3a). Second is the pyrochlore lattice with 3700 materials (Figs. 2b, 3b). The one-dimensional stub lattice is third with 3669 (Figs. 2c, 3c), followed by the "diamond chain"[4] lattice, a 1D chain of alternating one or two sites, with 2557 (Figs. 2d and 3d). Following this are the Lieb lattice with 1976 (Figs. 2e, 3e), the fluorite CaF_2 lattice (with both the Ca and F sites occupied by the same species) with 1330 (Figs. 2f, 3f), a diamond chain lattice with a transverse bond here referred to as the "Kite" lattice with 1,291 (Figs. 2g, 3g), the tetrahedron chain with 1131 (Figs. 2h, 3h), a honeycomb with an additional orbital connected to one vertex, which we refer to here as the "Stub Honeycomb" with 1049 (Figs. 2i, 3i), and the hyperkagome[44] lattice which is the edge net of the $SrSi_2$ lattice[45] has 930 (Figs. 2j, 3j).

In Table 2, we provide the abundances of elemental flatband sublattices being hosted by *s*, *p*, *d*, or *f* block elements on 1-, 2-, or 3-dimensional networks. In terms of composition, most identified flat band lattices are built of *p* block elements, followed by the *d* block, *s* block, and *f* block (see also Supplementary Figure 1 and Supplementary Note 4). This is likely biased by the contents of the database itself (e.g., Li is both the second most abundant element in the MP and the flat band catalog here, see Supplementary Figure 1 and Supplementary Note 4). It is also of interest to explore the role of chemical bonding in flat band formation; i.e., if covalent bonds may be more likely to form the relatively non-close-packed flat band lattices depicted in Fig. 2 than a metallic element—for example, oxygen makes up only 14.8% of elemental sublattices in the MP, but forms 37.5% of all flat band sublattices found here. We also observe a relatively uniform distribution of one-dimensional, two-dimensional, and three-dimensional flat band lattices. Only 20.8% of results contain a flat band with the most restrictive choice $\chi = 1.02$. All search results are available in a supplemental data sheet (see Supplementary Note 3).

Identifying flat band material families

Analysis of the identified flat band lattice materials reveals connections between several of these networks in terms of dimensionality and the character of the CLS. For example, many flat band networks arise from a similar interference mechanism as the kagome net: a ring with an even number of sites with each nearest-neighbor of the ring hopping to two adjacent sites within the ring. In Fig. 4, we show the relationship between various 1D, 2D, and 3D flat band lattice materials that fit this description. Starting with the XY_5 ($CaCu_5$-type) structure (Fig. 4b) of *AA* stacked bi-connected kagome layers, replacement of one or both connecting *Y* atoms with *Z* atoms yields the mono-connected (XY_4Z, Fig. 4c) and disconnected (XY_3Z_2, Fig. 4d) kagome flat band lattices, respectively. Further substitution of *Y* for *Z* to $XY_{2.5}Z_{2.5}$ results in a 1D kagome ladder flat band lattice (Fig. 4h). Converting *Z* to *X* in XY_4Z to obtain XY_2, different stackings (with slight distortion on *X* sites) produce the the *ABC* stacked ($MgCu_2$-type, C15) cubic laves phase pyrochlore flat band lattice (Fig. 4f) and the *AB* stacked ($MgZn_2$-type, C14) "znz" hexagonal laves phase flat band lattice (Fig. 4g). Shifting, substituting, and splitting sites in the XY_3Z_2 structure can result in the *XY* (CoSn-type) kagome flat band lattice (Fig. 4e), or the XY_6Z_6 ($MgFe_6Ge_6$-type) kagome flat band lattice (Fig. 4i). This can be considered a kagome "family" of systems: all can be thought of as distinct ways of connecting kagome lattices while maintaining destructive interference of the hopping around the hexagonal ring. As such, the CLS's of all lattices in Fig. 4 will consist of orbitals with alternating signs around the hexagonal ring. Further exploration of other motifs cataloged in the present search may provide insights into other flat band material families and how flat band changes across those classes.

Discussion

We have identified 108,161 sublattices hosting a structural motif that contains a flat band at the *s*-orbital model level in the MP, comprised of more than 31,635 unique lattices. These include motifs with a variety of potentially interesting bandstructure features, including isolated flat bands, linear and quadratic intersections with the flat band (including singularity of the wavefunction at intersection points[46]), and multiply degenerate flat bands. These lattices are categorized to the extent possible with current graph theory algorithms, allowing the identification of isomorphically equivalent flat band lattices in a majority of search results. The present graph theory-based approach enables further flexibility in the present search through its ability to identify distorted lattices and categorize them by their most symmetric forms. For example, as shown in Fig. 5a, $Al_6B_5O_18$ is identified to contain a hidden distorted oxygen star lattice amongst many clusters of oxygen atoms, the chromium sublattice of Cr_3AgO_8 can be considered a 3D distorted dice lattice (Fig. 5b), and the $Ba(Ag_3O_2)_2$ unit cell contains two distorted Lieb lattices of silver (Fig. 5c). This provides a significantly more general framework for classifying lattices than a purely geometric or symmetry-based method.

Beyond this classification at a model level, the present search also aids in identifying materials in different proximities to ideal models. A tight grouping of bond lengths ($d_{NN,max}/d_{NN}$ close to one) is more likely to represent a relatively undistorted lattice, and a large ratio $d_{NNN}/d_{NN,max}$ is less likely to overlook relevant hopping pathways. The shortest bond included, d_{NN}, should also be small to ensure *t* is a dominant energy scale (though it may be useful to relax this requirement in some systems, such as metal-organic frameworks). The robustness of a flat band to the inclusion of decreasing hopping strength with increasing bond length is another metric of the flat band model reliability. One might also seek simple materials with a minimal number of sites in the unit cell to minimize additional bands (examples of complex unit cells are provided in Supplementary Fig. 3 and discussed in Supplementary Note 6). Combining these criteria, we provide a curated list in the supplemental materials of 2759 systems with filtered values of key parameters: materials with 16 or fewer atoms per unit cell, $d_{NN} \leq 3.7$ Å, $d_{NN,max}/d_{NN} \leq 1.05$, $d_{NNN}/d_{NN,max} \geq 1.35$, and a negative energy per atom in the MP calculation are included. These criteria are designed to favor the appearance of robust flat bands in the material bandstructure; specific examples from this curated list in which the DFT manifests the tight-binding features are discussed in Supplementary Note 7 and shown in Supplementary Figs. 4–9. We emphasize that because the results are not guaranteed to represent the ideal *s*-orbital model when searching for flat band materials, this database is best used as an identification tool to generate a constrained list upon which to build a more sophisticated analysis.

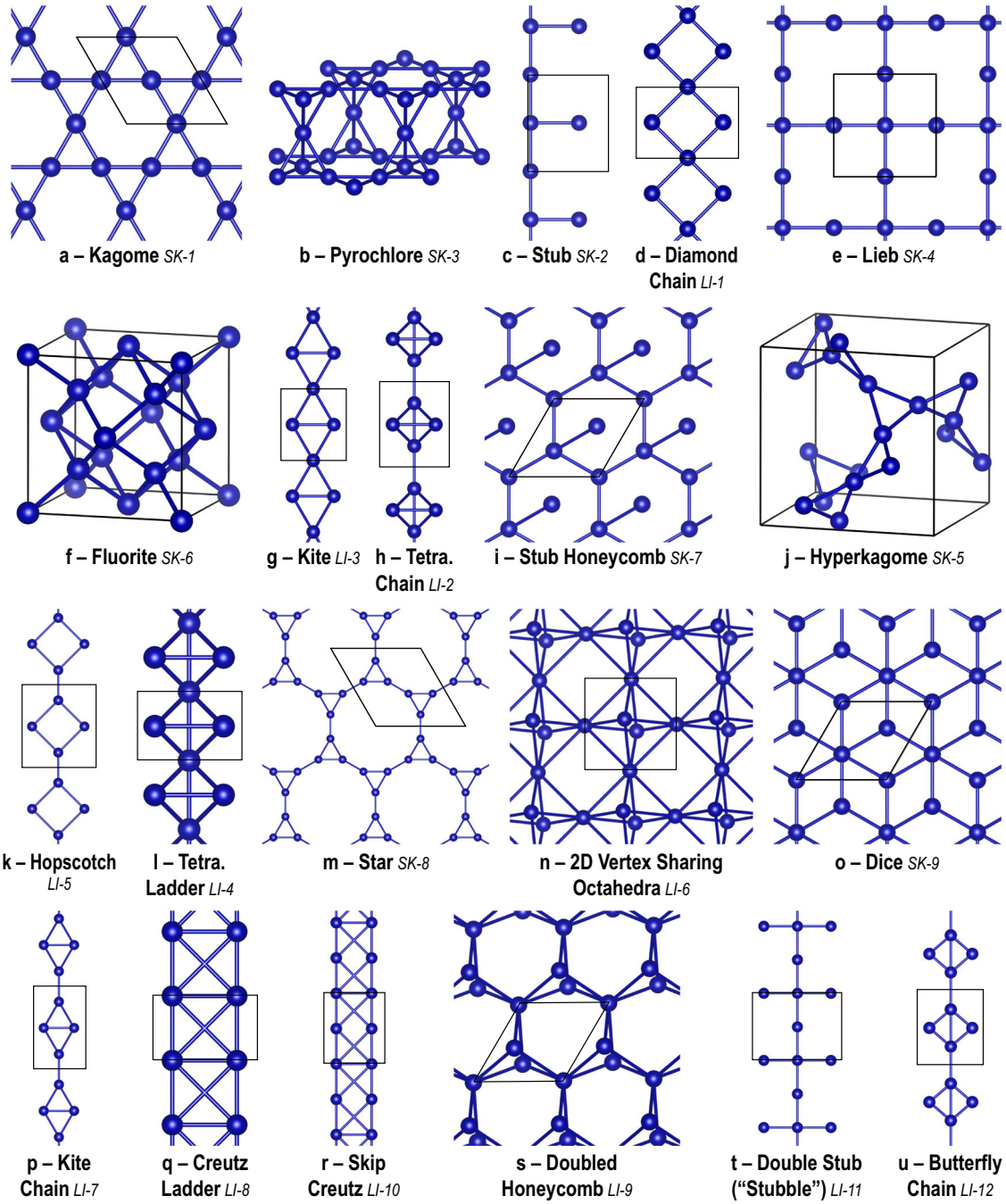

Fig. 2 | The twenty-one most common non-trivial flat band lattices. a–u Lattices identified by the present search are sorted in descending order of occurrence. The unit cell for each is shown with a solid black line. The lattice code of each lattice is indicated after the lattice name.

Despite overlooking many effects that could render the flat band dispersive, the complete, unfiltered results may be of use to group materials based on flat band motifs, enable further screening to find high quality flat band materials, and identify additional models for theoretical and artificial lattice investigations. For example, although this method does not include higher orbital angular momentum orbitals, in some cases this isotropic approximation is valid. For instance, in 2D lattices where crystal field splitting separates the p_z or d_{z^2} orbitals from all other orbitals, the tight-binding model retains the same symmetry as an *s*-orbital model and therefore the model bandstructure remains the same. Effective *s*-orbital models have also been used to describe the bandstructure of metal-organic or covalent-organic frameworks where a cluster of atoms acts as one effective s-orbital[47,48]. Further, in some cases, the local symmetries between orbitals on adjacent sites retain the frustration conditions of the *s*-orbital model (e.g., specific orbitals for the *d*-orbital kagome model, see Supplementary Information in ref. 14).

In other cases, however, a higher orbital angular momentum basis may be required to create flat bands, such as in the $\{p_x, p_y\}$ honeycomb model[49]. Beyond this, spin-orbit coupling (SOC) (relevant for topological features), further neighbor and anisotropic hopping, interaction effects, and orbitals on other sublattices are neglected (while orbitals on the considered sublattice are given equal self-energies). Mitigation of each of these can be pursued by appropriate elemental and structure filtering of the search results, as discussed in Supplementary Note 7. The coexistence of dispersive bands with the flat bands can also affect the accessible physics and should be considered when identifying flat band material candidates (and can give rise to interesting behavior itself[50,51]). In the future, this flat band search method could be extended to produce additional flat band

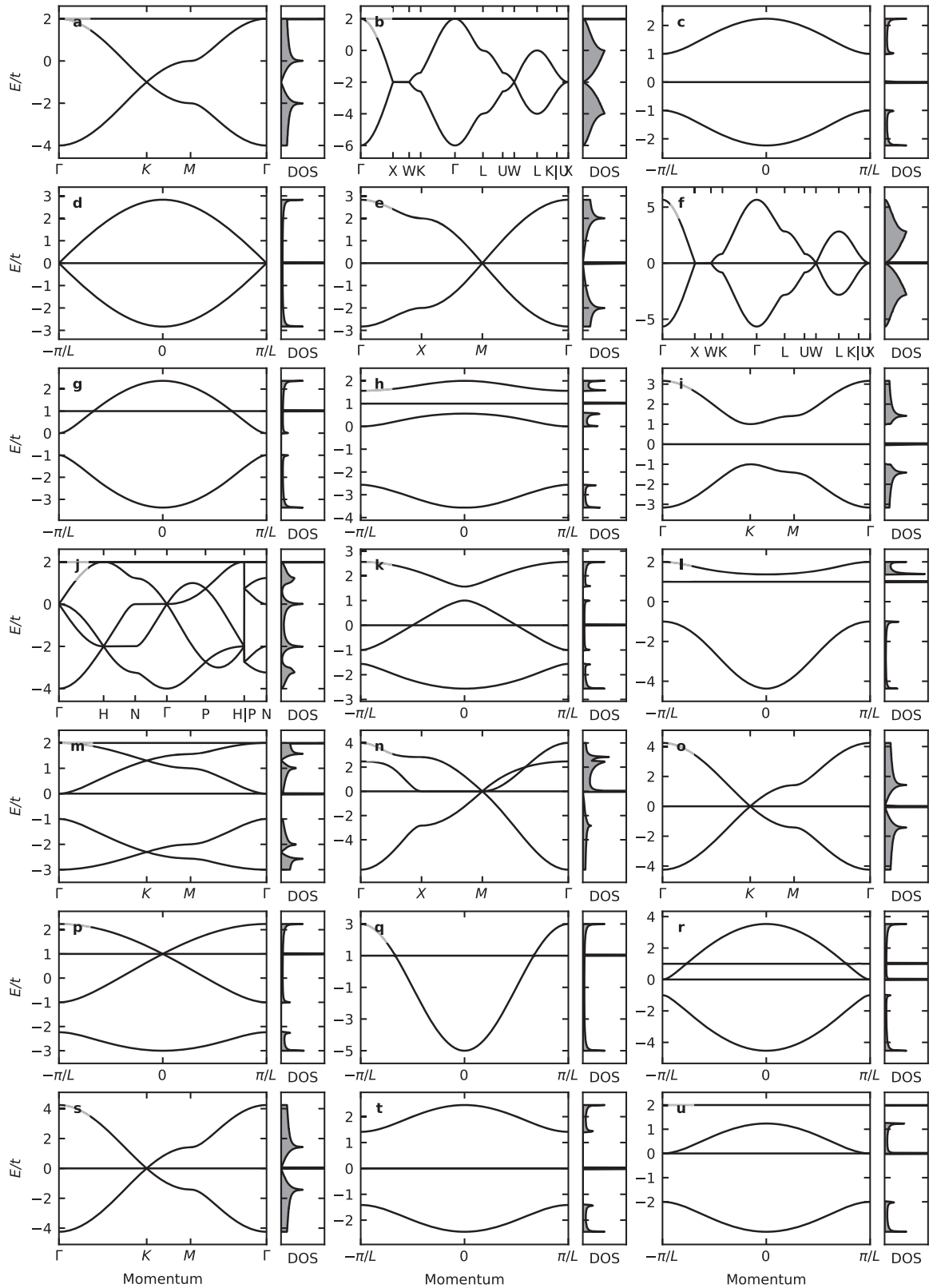

Fig. 3 | Bandstructure and density of states for the most common lattices. Bandstructures follow the same panel ordering **a**–**u** as presented in Fig. 2. The energy E is normalized by the hopping integral t. The right-hand sub-panels show the density of states (DOS).

models and more accurate results by including these effects. More sophisticated search algorithms are also of significant interest; in particular, comparison with recent geometry- and DFT-based catalogs[32,52,53] may provide additional insights for both theoretical models and identification of experimental materials targets. The development of tools to identify a material which realizes a complex model that is dependent on detailed orbital texture is an outstanding challenge to the field and worthy of significant future work.

Alternative methods for screening tight-binding models for candidate flat band systems could also be considered. Starting from ab initio density functional theory calculations for a material, one can manually construct an effective Hamiltonian with maximally localized Wannier functions[54] (though this is significantly more computationally intensive than the present approach). Other methods attempting to construct a tight-binding model database[55] or generate tight-binding models from ab initio calculations can also be considered[56–59]. Finally, we propose that this general framework of high-throughput tight-binding and graph isomorphism analysis can be applied to a broader range of materials searches, for example, in searching for systems with symmetry-protected band nodes, nodal points, or massless dispersions. The materials insight provided by those and the present flat band focused investigations may provide a theoretical and computational resource for identifying exotic phases in lattice systems and an experimental resource for selection of synthesis targets in both artificial lattice and material-based studies.

Table 2 | Sublattice Statistics

Property	No. Sublattices
All	468,378
Have F.B.	108,161
Curated	2958
s block	15,021
p block	65,050
d block	24,868
f block	3222
1D	35,537
2D	36,692
3D	36,558
Systre compatible	60,913
Systre incompatible	47,248

Statistics for general properties of elemental sublattices identified to contain flat band models.

Methods

Identification of nontrivial flat bands

We eliminate components (subsets of atoms and bonds in the periodic graph that do not connect via any hoppings to other components of the graph) that are completely isolated within the lattice—i.e., clusters of connected atoms that cannot hop infinitely far from any of the atoms in the cluster, as exemplified by the S sublattice in $Bi_2Rh_3S_2$ (Fig. 1h). As such a completely localized component of a crystal net will have no momentum dependent eigenvalues, this step identifies the number of "trivial' flat bands that will be present in the final bandstructure (those that would describe a

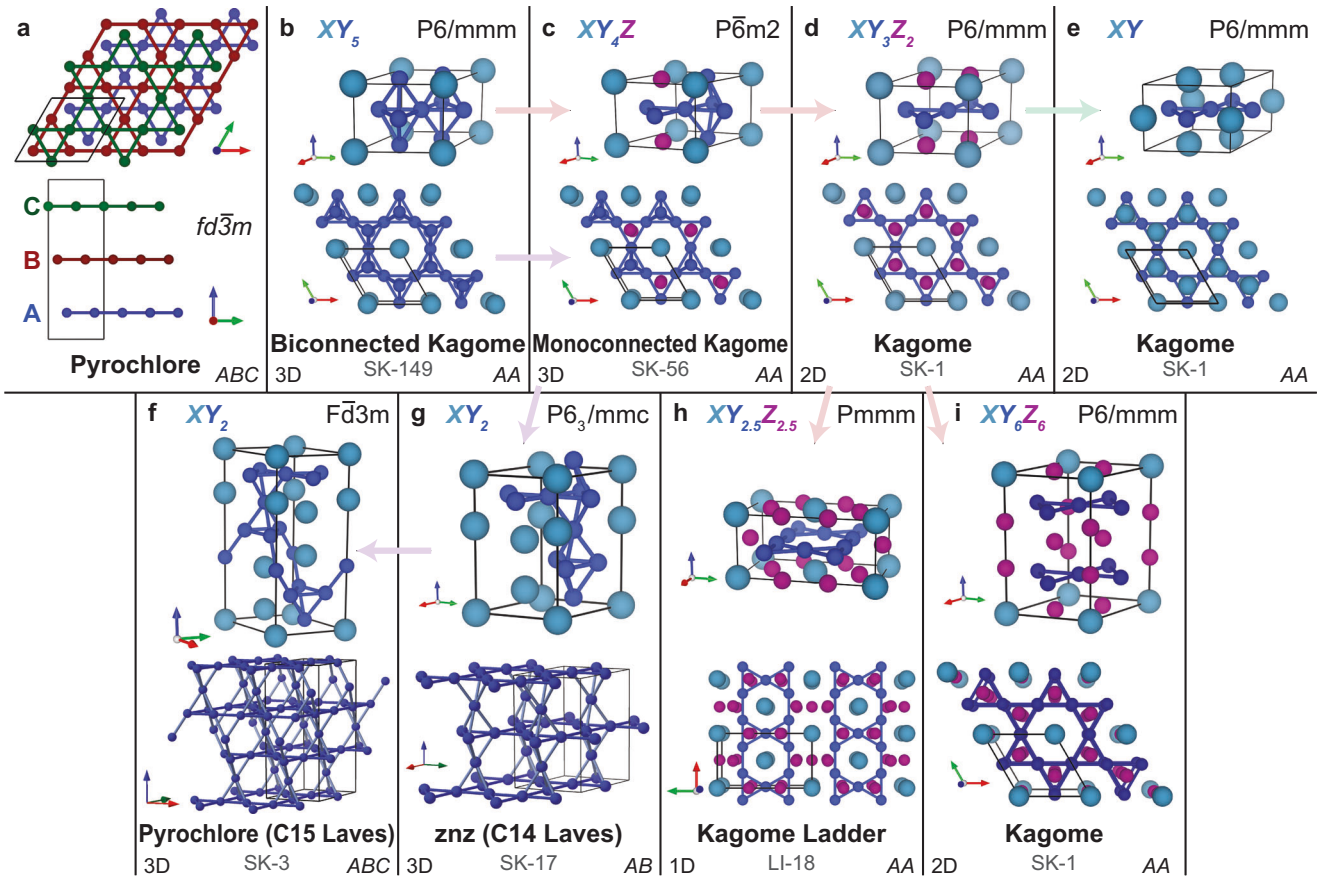

Fig. 4 | Relations between flat band lattices in the kagome families. a The pyrochlore *ABC* stacking of kagome lattices (interlayer sites not shown). **b** The $CaCu_5$ type structure, showing the 3D flat band *Y* sublattice. **c** By substituting one *Y* site from (**b**), a different 3D flat band lattice is obtained. **d** Substituting a second *Y* site creates the 2D kagome flat band lattice. **h** Substituting further to $XY_{2.5}Z_{2.5}$ creates a 1D version of the kagome lattice, referred to here as the "kagome ladder." **e** The *XY* kagome flat band lattice can be generated from (**d**) by shifting the corner *X* site and converting *Z* sites to *X* sites. **i** The XY_6Z_6 lattice is obtained from (**d**) by doubling the unit cell along the c-axis and splitting one *X* site into two *Z* sites. **g** The znz (C14 hexagonal Laves phase) 3D flat band lattice is created from (**c**) by changing to an *AB* stacking, substituting an *X* for a *Z*, and distorting two *X* sites. **f** By altering to an *ABC* stacking, the cubic C15 Laves pyrochlore lattice can be realized in the XY_2 system. The pyrochlore unit cell depicted in (**a**) and (**f**) is rotated such that the *c*-axis is along the conventional [111] direction to facilitate comparison amongst structures. Dimensionality is indicated in the lower left of each panel. Stacking order is indicated in the lower right of each panel. The lattice code of each lattice is indicated in the lower center of each panel.

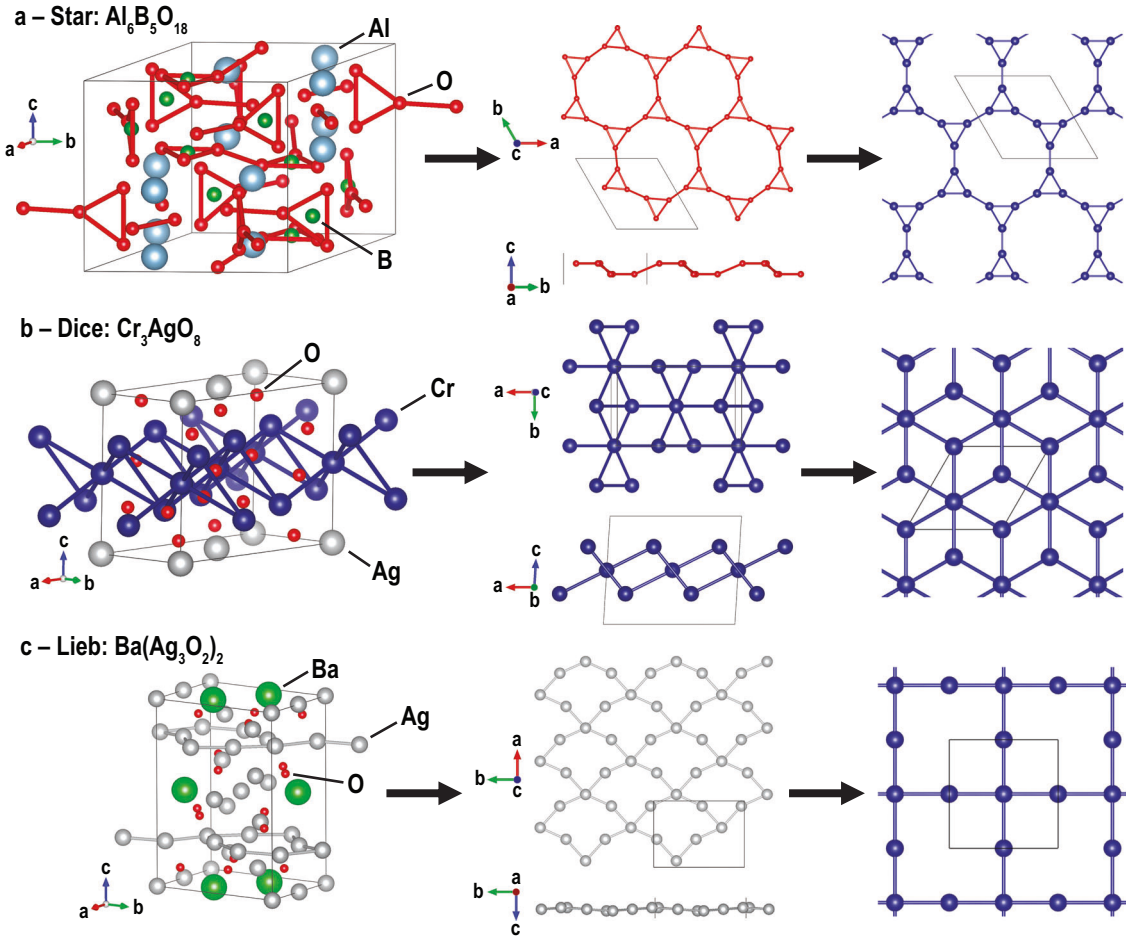

Fig. 5 | Distorted lattices and higher symmetry flat band lattices. a (left) Structure of $Al_6B_5O_{18}$, (center) its isolated oxygen star lattice, and (right) the topologically equivalent higher symmetry counterpart. **b** Structure of Cr_3AgO_8, its isolated chromium dice lattice, and undistorted form. **c** Structure of $Ba(Ag_3O_2)_2$, its isolated silver Lieb lattice, and undistorted form.

lattice of decoupled molecular states). All remaining flat bands must then admit a description via the construction of nontrivial CLS due to frustrated hopping, e.g., the Rh sublattice in $Bi_2Rh_3S_2$ in Fig. 1g (see Supplementary Note 1).

Discarding sites in the lattice determined to be trivially localized, we then calculate the eigenvalues of the remaining tight-binding Hamiltonian on a $16 \times 16 \times 16$ grid mesh of k points in the Brillouin zone. We bin the eigenvalues with bins one-thousandth of the total range of the band-structure. A flat band is identified for any energy bin that contains an eigenvalue in that bin at every calculated k point. Thus, a band must be no more dispersive than 0.1% of the total dispersion of the bandstructure across the entire Brillouin zone. Such a search is presented here for $\chi = 1.02$, 1.05, 1.1, 1.2, and 1.4 in order to capture lattices with a wide range of distortion and connectivity. $\chi = 1.02$ was used as the lowest cutoff to allow for up to 2% bond distortions to be considered identical, and to accommodate rounding errors in the relaxed structure ($\chi = 1.4$ was used as the largest cutoff to avoid inclusion of bonds along the hypotenuse of three atoms in a right triangle).

Lattice classification

We attempt to categorize the identified lattices into groups of identical crystal nets (e.g., all kagome lattices). As the band flatness in a tight-binding model with uniform hopping originates from the topology of the periodic graph that describes the connectivity of orbitals, lattices identified by this search can be categorized by their crystal net isomorphisms. As such, a highly distorted lattice (Fig. 1d) will have identical bandstructure with its undistorted version (Fig. 1i), assuming the connectivity of the orbitals is the same. To classify lattices, we use the method of barycentric placement implemented by Systre[43], which associates a Systre "key" unique to each periodic graph, the ideal symmetry group of the graph, and its dimensionality (Fig. 1j). The limitation of this method is that for ~40% of flat band lattices, two or more vertices' barycentric locations are identical which prevents those lattices from being classified according to this scheme. For these, we group lattices based on lattice invariants including the number of atomic sites, the number and energies of the flat bands, and the approximate range of the energy eigenstates (see Supplemental Note 2). Each unique flat band lattice type identified in this work is assigned a lattice ID number beginning with "LI-" or "SK-" for those classified by lattice invariant or systre key, respectively. Following this prefix, a number is assigned based on the frequency of occurrence of the lattice in descending order.

Code and databases used

We obtain crystal structures from the MP[42] (database version May 13, 2021). Structural analysis is performed with the pymatgen python library[60,61]. Tight-binding models are calculated with the pythTB python library[62]. Crystal net classification and analysis are performed with Systre[43]. Additional analysis is performed with standard python libraries, Numpy, and Scipy. A curated list of classified results is included in the Supplemental Materials.

Data availability

The search results and curated list are available as a supplementary data sheet. See Supplementary Note 3 for more information.

Code availability

Code used to generate tight-binding models and identify/classify flat bands is available at https://github.com/pmneves7/Crystal-Net-Flat-Bands/tree/main.

Received: 10 January 2023; Accepted: 30 January 2024;
Published online: 20 February 2024

References

1. Micnas, R., Ranninger, J. & Robaszkiewicz, S. Superconductivity in narrow-band systems with local nonretarded attractive interactions. *Rev. Mod. Phys.* **62**, 113 (1990).
2. Mielke, A. Ferromagnetic ground states for the Hubbard model on line graphs. *J. Phys. A Math. Gen.* **24**, L73 (1991).
3. Sethi, G., Zhou, Y., Zhu, L., Yang, L. & Liu, F. Flat-band-enabled triplet excitonic insulator in a diatomic kagome lattice. *Phys. Rev. Lett.* **126**, 196403 (2021).
4. Aoki, H. Theoretical possibilities for flat band superconductivity. *J. Supercond. Nov. Magn.* **33**, 2341–2346 (2020).
5. Tang, E., Mei, J.-W. & Wen, X.-G. High-temperature fractional quantum hall states. *Phys. Rev. Lett.* **106**, 236802 (2011).
6. Bergholtz, E. J. & Liu, Z. Topological flat band models and fractional Chern insulators. *Int. J. Mod. Phys. B* **27**, 1330017 (2013).
7. Volovik, G. E. Graphite, graphene, and the flat band superconductivity. *JETP Lett.* **107**, 516–517 (2018).
8. Cao, Y. et al. Unconventional superconductivity in magic-angle graphene superlattices. *Nature* **556**, 43–50 (2018).
9. Cao, Y. et al. Correlated insulator behaviour at half-filling in magic-angle graphene superlattices. *Nature* **556**, 80–84 (2018).
10. Park, J. M., Cao, Y., Watanabe, K., Taniguchi, T. & Jarillo-Herrero, P. Flavour Hund's coupling, Chern gaps and charge diffusivity in moiré graphene. *Nature* **592**, 43–48 (2021).
11. Li, H. et al. Imaging moiré flat bands in three-dimensional reconstructed WSe_2/WS_2 superlattices. *Nat. Mater.* **20**, 945–950 (2021).
12. Zhang, Z. et al. Flat bands in twisted bilayer transition metal dichalcogenides. *Nat. Phys.* **16**, 1093–1096 (2020).
13. Balents, L., Dean, C. R., Efetov, D. K. & Young, A. F. Superconductivity and strong correlations in moiré flat bands. *Nat. Phys.* **16**, 725–733 (2020).
14. Kang, M. et al. Topological flat bands in frustrated kagome lattice CoSn. *Nat. Commun.* **11**, 1–9 (2020).
15. Wakefield, J. P. et al. Three-dimensional flat bands in pyrochlore metal $CaNi_2$. *Nature* **623**, 301–306 (2023).
16. Kollár, A. J., Fitzpatrick, M., Sarnak, P. & Houck, A. A. Line-graph lattices: Euclidean and non-euclidean flat bands, and implementations in circuit quantum electrodynamics. *Commun. Math. Phys.* **376**, 1909–1956 (2020).
17. Taie, S. et al. Coherent driving and freezing of bosonic matter wave in an optical lieb lattice. *Sci. Adv.* **1**, e1500854 (2015).
18. Leykam, D., Andreanov, A. & Flach, S. Artificial flat band systems: from lattice models to experiments. *Adv. Phys. X* **3**, 1473052 (2018).
19. Lieb, E. H. Two theorems on the Hubbard model. *Phys. Rev. Lett.* **62**, 1201 (1989).
20. Sutherland, B. Localization of electronic wave functions due to local topology. *Phys. Rev. B* **34**, 5208 (1986).
21. Bergman, D. L., Wu, C. & Balents, L. Band touching from real-space topology in frustrated hopping models. *Phys. Rev. B* **78**, 125104 (2008).
22. Derzhko, O., Richter, J. & Maksymenko, M. Strongly correlated flat-band systems: The route from Heisenberg spins to Hubbard electrons. *Int. J. Mod. Phys. B* **29**, 1530007 (2015).
23. Arai, M., Tokihiro, T., Fujiwara, T. & Kohmoto, M. Strictly localized states on a two-dimensional Penrose lattice. *Phys. Rev. B* **38**, 1621 (1988).
24. Li, Z. et al. Realization of flat band with possible nontrivial topology in electronic kagome lattice. *Sci. Adv.* **4**, eaau4511 (2018).
25. Yin, J.-X. et al. Negative flat band magnetism in a spin–orbit-coupled correlated kagome magnet. *Nat. Phys.* **15**, 443–448 (2019).
26. Kang, M. et al. Dirac fermions and flat bands in the ideal kagome metal FeSn. *Nat. Mater.* **19**, 163–169 (2020).
27. Liu, Z. et al. Orbital-selective Dirac fermions and extremely flat bands in frustrated kagome-lattice metal CoSn. *Nat. Commun.* **11**, 1–7 (2020).
28. Meier, W. R. et al. Flat bands in the CoSn-type compounds. *Phys. Rev. B* **102**, 075148 (2020).
29. Li, M. et al. Dirac cone, flat band and saddle point in kagome magnet YMn_6Sn_6. *Nat. Commun.* **12**, 1–8 (2021).
30. Han, M. et al. Evidence of two-dimensional flat band at the surface of antiferromagnetic kagome metal FeSn. *Nat. Commun.* **12**, 1–10 (2021).
31. Ye, L. et al. Hopping frustration-induced flat band and strange metallicity in a kagome metal. *Nat. Phys.* https://doi.org/10.1038/s41567-023-02360-5 (2024).
32. Regnault, N. et al. Catalogue of flat-band stoichiometric materials. *Nature* **603**, 824–828 (2022).
33. Pal, B. Nontrivial topological flat bands in a diamond-octagon lattice geometry. *Phys. Rev. B* **98**, 245116 (2018).
34. Mondaini, R., Batrouni, G. G. & Grémaud, B. Pairing and superconductivity in the flat band: Creutz lattice. *Phys. Rev. B* **98**, 155142 (2018).
35. Kuno, Y. Extended flat band, entanglement, and topological properties in a Creutz ladder. *Phys. Rev. B* **101**, 184112 (2020).
36. He, Y. et al. Flat-band localization in Creutz superradiance lattices. *Phys. Rev. Lett.* **126**, 103601 (2021).
37. Miyahara, S., Kubo, K., Ono, H., Shimomura, Y. & Furukawa, N. Flat-bands on partial line graphs—systematic method for generating flat-band lattice structures–. *J. Phys. Soc. Jpn.* **74**, 1918–1921 (2005).
38. Ma, D.-S. et al. Spin-orbit-induced topological flat bands in line and split graphs of bipartite lattices. *Phys. Rev. Lett.* **125**, 266403 (2020).
39. Ogata, T., Kawamura, M. & Ozaki, T. Methods for constructing parameter-dependent flat-band lattices. *Phys. Rev. B* **103**, 205119 (2021).
40. Călugăru, D. et al. General construction and topological classification of crystalline flat bands. *Nat. Phys.* **18**, 185–189 (2022).
41. Chiu, C. S., Carroll, A. N., Regnault, N. & Houck, A. A. Line-graph-lattice crystal structures of stoichiometric materials. *Phys. Rev. Res.* **4**, 023063 (2022).
42. Jain, A. et al. Commentary: The materials project: A materials genome approach to accelerating materials innovation. *APL Mater.* **1**, 011002 (2013).
43. Delgado-Friedrichs, O. & O'Keeffe, M. Identification of and symmetry computation for crystal nets. *Acta Cryst. A* **59**, 351–360 (2003).
44. Lawler, M. J., Paramekanti, A., Kim, Y. B. & Balents, L. Gapless spin liquids on the three-dimensional hyperkagome lattice of $Na_4Ir_3O_8$. *Phys. Rev. Lett.* **101**, 197202 (2008).
45. Friedrichs, O. D., O Keeffe, M. & Yaghi, O. M. Three-periodic nets and tilings: regular and quasiregular nets. *Acta Cryst. A* **59**, 22–27 (2003).
46. Rhim, J.-W. & Yang, B.-J. Classification of flat bands according to the band-crossing singularity of Bloch wave functions. *Phys. Rev. B* **99**, 045107 (2019).
47. Jiang, W., Ni, X. & Liu, F. Exotic topological bands and quantum states in metal-organic and covalent-organic frameworks. *Acc. Chem. Res.* **54**, 416–426 (2021).
48. Wang, X.-B. et al. A p-orbital honeycomb-kagome lattice realized in a two-dimensional metal-organic framework. *Commun. Chem.* **6**, 73 (2023).
49. Wu, C., Bergman, D., Balents, L. & Sarma, S. D. Flat bands and Wigner crystallization in the honeycomb optical lattice. *Phys. Rev. Lett.* **99**, 070401 (2007).

50. Rhim, J.-W. & Yang, B.-J. Singular flat bands. *Adv. Phys. X* **6**, 1901606 (2021).
51. Deng, S., Simon, A. & Köhler, J. A" flat/steep band" model for superconductivity. *Int. J. Mod. Phys. B* **19**, 29–36 (2005).
52. Meschke, V., Gorai, P., Stevanovic, V. & Toberer, E. S. Search and structural featurization of magnetically frustrated kagome lattices. *Chem. Mater.* **33**, 4373–4381 (2021).
53. Jovanovic, M. & Schoop, L. M. Simple chemical rules for predicting band structures of kagome materials. *J. Am. Chem. Soc.* **144**, 10978–10991 (2022).
54. Marzari, N., Mostofi, A. A., Yates, J. R., Souza, I. & Vanderbilt, D. Maximally localized wannier functions: Theory and applications. *Rev. Mod. Phys.* **84**, 1419 (2012).
55. Garrity, K. F. & Choudhary, K. Database of Wannier tight-binding Hamiltonians using high-throughput density functional theory. *Sci. Data* **8**, 1–10 (2021).
56. Unke, O. et al. Se (3)-equivariant prediction of molecular wavefunctions and electronic densities. *Adv. Neural Inf. Process.* **34**, 14434–14447 (2021).
57. Zhang, L. et al. Equivariant analytical mapping of first principles Hamiltonians to accurate and transferable materials models. *npj Comput. Mater.* **8**, 158 (2022).
58. Nakhaee, M., Ketabi, S. & Peeters, F. Machine learning approach to constructing tight binding models for solids with application to BiTeCl. *J. Appl. Phys.* **128**, 215107 (2020).
59. Vitale, V. et al. Automated high-throughput wannierisation. *npj Comput. Mater.* **6**, 66 (2020).
60. Ong, S. P. et al. Python materials genomics (pymatgen): a robust, open-source Python library for materials analysis. *Comput. Mater. Sci.* **68**, 314–319 (2013).
61. Ong, S. P. et al. The materials application programming interface (API): a simple, flexible and efficient API for materials data based on representational state transfer (REST) principles. *Comput. Mater. Sci.* **97**, 209–215 (2015).
62. Yusufaly, T., Vanderbilt, D. & Coh, S. Tight-binding formalism in the context of the PythTB package (2013).
63. O'Keeffe, M., Peskov, M. A., Ramsden, S. J. & Yaghi, O. M. The reticular chemistry structure resource (RCSR) database of, and symbols for, crystal nets. *Acc. Chem. Res.* **41**, 1782–1789 (2008).

Acknowledgements

We thank J. Cano, B.-J. Yang, T. Suzuki, G. Tritsaris, D. Tabor, and A. Aspuru-Guzik for useful discussions. This research is funded in part by the Gordon and Betty Moore Foundation EPiQS Initiative, through Grant GBMF9070 to J.G.C. (computation), NSF grant DMR-2104964 (statistical analysis), and AFOSR grant FA9550-22-1-0432 (crystallographic analysis). H.N. and L.Y. acknowledge support by the STC Center for Integrated Quantum Materials, NSF grant number DMR-1231319. This work was performed in part at the Aspen Center for Physics, which is supported by National Science Foundation grant PHY-1607611.

Author contributions

P.M.N. wrote the code with input from J.P.W. and S.F., P.M.N., J.P.W., and S.F. interpreted the search results with input from L.Y. H.N., J.P.W., and L.Y. performed preliminary geometry-based searches. J.G.C. supervised the project. All authors analyzed the results and contributed to writing the manuscript.

Competing interests

The authors declare no competing interests.

Additional information

Supplementary information The online version contains supplementary material available at https://doi.org/10.1038/s41524-024-01220-x.

Correspondence and requests for materials should be addressed to Joseph G. Checkelsky.